# Dynamics of Photogenerated Charge Carriers in $WO_3/BiVO_4$ Heterojunction Photoanodes



| | |
|---|---|
| Journal: | *The Journal of Physical Chemistry* |
| Manuscript ID: | jp-2015-05128c.R1 |
| Manuscript Type: | Article |
| Date Submitted by the Author: | n/a |





| | |
|---|---|
| Complete List of Authors: | Grigioni, Ivan; University of Milan, Department of Chemistry<br>Stamplecoskie, Kevin; University of Notre Dame, Chemistry<br>Selli, Elena; University of Milan, Department of Chemistry<br>Kamat, Prashant; University of Notre Dame, Notre Dame, USA, Department of Chemistry & Biochemistry |

# Dynamics of Photogenerated Charge Carriers in $WO_3/BiVO_4$ Heterojunction Photoanodes

Ivan Grigioni,[†] Kevin G. Stamplecoskie,[‡] Elena Selli,*[,†] and Prashant V. Kamat[‡]

[†]Dipartimento di Chimica, Università degli Studi di Milano, via Golgi 19, I-20133 Milano, Italy

[‡]Radiation Laboratory, University of Notre Dame, Notre Dame, Indiana 46556, USA

* Corresponding Author. Phone +39 02 50314237. Fax: +39 02 50314300. E-mail: elena.selli@unimi.it.

**ABSTRACT**: Bismuth vanadate ($BiVO_4$) with a band gap of ~2.4 eV has emerged as one of the visible photocatalysts that can absorb light below 520 nm. The electron/hole pairs that are generated following $BiVO_4$ band gap excitation are effective for water splitting, especially when $BiVO_4$ is combined with other metal oxides such as $WO_3$. We report a solution processed method for designing transparent $WO_3/BiVO_4$ heterojunction electrodes and observe a synergistic effect on the photoelectrochemical activity of $WO_3/BiVO_4$, with the combined system performing dramatically better than either individual components. Using ultrafast transient absorption spectroscopy the electronic interaction between $WO_3$ and excited $BiVO_4$ is elucidated. Moreover, the photocatalytic reduction of thionine by $WO_3/BiVO_4$ as well as by each individual oxide component is used to track electron injection processes and determine the energetics of the studied systems. In the composite $WO_3/BiVO_4$ film a shifted quasi-Fermi level results, due to electronic equilibration between the two materials. The better performance of $WO_3/BiVO_4$ heterojunction electrodes is thus a consequence of the electron injection from $BiVO_4$ into $WO_3$, followed by back electron transfer from $WO_3$ to the holes in $BiVO_4$.

## 1. INTRODUCTION

Conversion and storage of solar energy in the form of fuels, such as photocatalytic splitting of water to generate hydrogen, have attracted increasing interest during the last two decades.[1,2] Semiconductor materials that are active under visible light[3] and other narrow band gap oxide semiconductors[4,5] have been extensively studied as possible photocatalysts. However, the stability and conversion efficiency that are needed for commercial application have not yet been achieved.

The stability of metal oxides such as $BiVO_4$ and $WO_3$ over a wide pH range and their ability to absorb high energy visible photons have attracted the attention of researchers to explore their photocatalytic properties towards the water splitting reaction.[6–8] These two semiconductors have band gaps of ~ 2.7[9] and 2.4[10,11] eV, respectively. Continued efforts to improve the photoelectrochemical performance of these materials have been made through surface modification,[12,13] doping[14,15] or nanostructured morphology,[16–18] as well as by using them in conjunction with oxygen evolution catalysts.[19–21]

Coupling of $BiVO_4$ with $WO_3$ offers an interesting approach to achieve better charge separation and thus improve the overall performance of the photocatalytic system.[22–25] Type II band alignment in these two semiconductor systems allows electrons from photoexcited $BiVO_4$ to be transferred into $WO_3$ and holes getting accumulated at $BiVO_4$. The decreased charge carrier recombination in the coupled system ensures better photoelectrochemical properties, similar to the spatial charge separation that occurs in natural photosynthetic systems.[26] Efforts are continuing to achieve photoconversion efficiencies close to the theoretical limit of these two materials.[27] On the other hand, little work has been done on understanding the charge carrier dynamics occurring in $BiVO_4$ and the interfacial charge separation in $WO_3/BiVO_4$ heterojunction electrodes.

Transient absorption spectroscopy has been recently employed to investigate the dynamics of photogenerated holes and electrons in $TiO_2$, $Fe_2O_3$, $WO_3$ and $BiVO_4$ photoanodes. For example, Durrant and co-workers[28–31] found that the application of an anodic bias allows the generation of holes with lifetime on the order of 100 ms to seconds, long enough to allow four-electron water oxidation. Although the dynamics of charge carriers with shorter timescale has been investigated in single oxide electrodes,[32,33] charge separation in coupled systems has yet to be explored fully.[34]

In the present work, femtosecond transient absorption spectroscopy is employed to investigate the electron injection dynamics from photoexcited $BiVO_4$ to $WO_3$ in the $WO_3/BiVO_4$ coupled system. A citrate-based synthesis employed to make transparent $WO_3$ films allowed us to achieve sufficient transparency for spectroscopic investigation. Furthermore, the effective charge separation in the coupled system was also probed through thionine reduction and the estimation of the apparent Fermi level of the photocatalyst assembly.

## 2. EXPERIMENTAL SECTION

**2.1. Materials.** The following chemicals were employed in the present work: tungsten(VI) ethoxide 99.8% (5% w/v in ethanol), ammonium vanadium oxide, bismuth(III) nitrate pentahydrate ACS 98%, benzyl alcohol ACS 99% (Alpha Aesar); ethyl cellulose (MP Biomedics); poly(vinyl alcohol) >99%, citric acid 99% (Aldrich); glacial acetic acid, anhydrous sodium sulfate and sodium sulphite (Fisher Scientific).

**2.2. Photoelectrodes preparation.** $WO_3$ was prepared as follows. 1.0 mL of tungsten ethoxide, 5 wt% in ethanol, was added to 42 mg of citric acid acting as stabilizer. Once citric acid was completely dissolved, benzyl alcohol (0.3 mL) and ethyl cellulose (40 mg) were added to the solution and stirred overnight to allow the complete dissolution of ethyl

cellulose. The so obtained paste is stable for several weeks. Fluorine-doped tin oxide (FTO) glass (Pilkington Glass, TEC-7, thickness 2 mm) was coated with the paste by spin coating at 6000 rpm for 30 s. Prior to deposition, the FTO glass was cleaned by 30 min-long sonication in a soap solution, in ethanol and finally in water. After coating, the film was dried for 1 h at 80°C and then annealed for 8 h at 500°C.

Bismuth vanadate films were prepared as reported elsewhere.[35] In a typical synthesis, 0.002 mol of $Bi(NO_3)_3$ and $NH_4VO_3$ were added to 6 mL of $HNO_3$ 23.3% containing 0.004 mol of citric acid. The mixture was stirred overnight to allow dissolution of the precursor. A denser paste was obtained by adding 0.04 g of polyvinyl alcohol and 0.25 mL of acetic acid to 1.0 mL of the above solution. A $BiVO_4$ layer was obtained by spin coating the paste at 4000 rpm for 30 s on clean FTO. The so obtained film was then dried for 1 h at 80°C and annealed for 8 h at 500°C.

The $WO_3/BiVO_4$ combined film was prepared by coating with the $BiVO_4$ dense paste a $WO_3$ electrode (prepared as described before, dried for 1 h at 80°C and annealed for 1 h at 500°C). Then the composite film underwent the same thermal treatment used for single material films.

**2.3. Optical, morphological and photoelectrochemical measurements.** Images showing the morphology and the cross section of the electrodes were obtained using a FEI Magellan-400 field emission scanning electron microscope (FESEM). UV-visible absorption spectra were recorded using a Varian Cary 50 Bio spectrophotometer. The crystalline phase of the materials was determined through XRPD analysis using a Philips PW1820 with Cu Kα radiation at 40 mA and 40 kV. Photoelectrochemical (PEC) measurements were carried out using a three electrode cell with an Ag/AgCl (3.0 M NaCl) reference electrode, a platinum gauze as a counter electrode and a Princeton Applied Research 2263 (PARstat) potentiostat. The light source was a 300 W Xe lamp with an AM 1.5G illumination (1 sun). A 0.5 M

$Na_2SO_4$ aqueous solution was used in electrochemical measurements. The potential *vs.* Ag/AgCl was converted into the RHE scale using the following equation: $E_{RHE} = E_{AgCl} + 0.059\ pH + E^{o}_{AgCl}$, with $E^{o}_{AgCl}$ (3.0 M KCl) = 0.210 V at 25°C.

Incident photon to current efficiency (IPCE) measurements were carried out with a set-up similar to that of PEC experiments, with a Bausch and Lomb grating monochromator placed between the Xe lamp and the sample. A 1.23 V bias *vs.* RHE was applied and the current was measured with a 10 nm step, within the 350 and 600 nm range. The incident light power was measured at each wavelength using a calibrated photodiode connected to a Keithley 617 electrometer. The IPCE was calculated at each wavelength λ (nm) using the following equation:

$$IPCE = \frac{[1240 \times J]}{P_{\lambda} \times \lambda} \times 100$$

where $J$ is the photocurrent density (mA $cm^{-2}$) and $P_{\lambda}$ (mW $cm^{-2}$) is the power of the monochromatic light at λ.

**2.4. Transient absorption spectroscopy.** Femtosecond transient absorption spectroscopy was used to follow the early evolution of photogenerated charge carriers in the two separate semiconductors and to track charge transfer in the $WO_3/BiVO_4$ heterojunction. Transient absorption measurements were recorded using a system based on a Ti:sapphire laser source (Clark MXR CPA-2010) generating pulses centered at 775 nm with a FWHM of 130 fs and 1 kHz repetition rate. 95% of the laser pulse was frequency doubled to λ = 387 nm and used as pump, while the remaining 5% was focused on a $CaF_2$ crystal to generate the white light probe. The detector used was a Helios transient absorption system from Ultrafast Systems. A pump energy density of 40 μJ $cm^{-2}$ was used during all experiments. Transient absorption

spectra were recorded within a 1400 ps scale in the 400-800 nm range and fitted with different models discussed in detail in the text.

**2.5. Photocatalytic thionine reduction.** Monochromatic light at 400 nm and 8 mW intensity was used in thionine (TH) reduction experiments. The light source was a 200 W Xe lamp equipped with a water filter and a monochromator (the same used for IPCE measurements). The light power intensity was always checked using a Thorlab PM100A power meter with a S120VC photodiode. The irradiated area (30 $mm^2$) was controlled using an iris. The irradiation wavelength was chosen to minimize TH self-reduction from its excited state. The absorption spectrum of TH has a minimum at 400 nm; on the other hand $WO_3$ and $BiVO_4$ have similar photoelectrochemical properties in this wavelength region. The films were placed in a 10 mm quartz cuvette containing 5 mL of ethanol and 25 μL of 5 mM TH solution in ethanol. Before starting irradiation, the solution was purged for 2 h with $N_2$, which was previously saturated with ethanol vapors in order to prevent evaporation of the solvent from the solution in the cuvette.

## 3. RESULTS AND DISCUSSION

**3.1. Characterization of oxide films deposited on transparent electrodes.** The absorption spectra of the three oxide films that were employed in the present investigation are shown in Figure 1. The $WO_3$ film with its band gap of ~ 2.7 eV shows good transparency in the visible. Relatively small absorption is seen below 450 nm. The $BiVO_4$ film and the $WO_3/BiVO_4$ coupled film exhibit an absorption onset around 500 nm (Figure 1). Residual absorption is seen above 550 nm, mainly due to light scattering.

These films were further characterized with Scanning Electron Microscopy (SEM). The $WO_3$ films (top view) is composed of *ca.* 17 nm diameter particles (Figure 2A). The cross section analysis (Figure 2C) shows the mesoporous architecture of the $WO_3$ layer with a

thickness of ~ 210 nm. The top view of the $WO_3/BiVO_4$ film in SEM analysis (Figure 2B) shows an aggregated network of particles, with morphological features similar to those reported for $BiVO_4$ films earlier.[36] The cross section of the $WO_3/BiVO_4$ coupled film (Figure 2D) shows sequential layering of $WO_3$ and $BiVO_4$. The thickness of $BiVO_4$ in this film was *ca.* 40 nm. The cross section image further ensures that the surface of the underlying $WO_3$ layer is fully covered by the $BiVO_4$ layer.

The X-ray powder diffraction patterns of the $WO_3$, $BiVO_4$ and $WO_3/BiVO_4$ electrodes (annealed for 8 h at 500°C) are reported in the Supporting Information (SI), together with that of cleaned FTO, for comparison (see Figure SI1 in the SI). Both individual materials fit well with monoclinic structures (JCPDS 05-0363 for $WO_3$ and JCPDS 75-1867 for $BiVO_4$). The combined electrode shows the reflection patterns of both monoclinic materials.

**3.2. Photoelectrochemical properties of individual and combined films.** We first evaluated the photoresponse of these three oxide electrodes in a photoelectrochemical (PEC) cell by employing them individually as a photoanode. The Pt electrode served as a counter electrode, Ag/AgCl served as reference along with 0.5 M $Na_2SO_4$ (pH 7) as electrolyte medium. The photoanode was subjected to backside irradiation (through FTO) with AM 1.5G simulated solar light. Both $BiVO_4$ and $WO_3$ semiconductors are stable at neutral pH and no noticeable degradation was observed during irradiation. The linear sweep voltammetry profiles obtained with the three electrodes under irradiation are shown in Figure 3.

This figure evidences that the electrodes require an external bias (>1 V *vs*. RHE) to exhibit photocurrent. The photocurrent recorded with the $WO_3/BiVO_4$ electrode was greater than those seen with the two individual $WO_3$ and $BiVO_4$ electrodes. At 1.23 V (*vs*. RHE) the current density was 0.35 mA $cm^{-2}$ for $BiVO_4$, 0.25 mA $cm^{-2}$ for $WO_3$ and 1.0 mA $cm^{-2}$ for the $WO_3/BiVO_4$ electrode. At this fixed applied potential, the $WO_3$ electrode generated slightly lower current than the $BiVO_4$ electrode. Considering that $BiVO_4$ harvests more light than

$WO_3$, since the band gap of $BiVO_4$ is narrower, the $WO_3$ photoelectrode showed higher efficiency in converting light into current. The low photocurrent generated by the $BiVO_4$ photoanode alone is attributed to the poor charge separation and interfacial charge transfer properties of this semiconductor material.[24]

A significant increase in the photocurrent is seen when $BiVO_4$ is coupled with $WO_3$. The enhanced photocurrent of the $WO_3/BiVO_4$ electrode arises from the improved charge separation as the electrons are transferred from $BiVO_4$ to $WO_3$. The conduction and valence bands of $BiVO_4$, which are more negative in energy than those of $WO_3$ (see Scheme SI1 in the SI), facilitate such charge separation. This in turn decreases the recombination rate typical of $h^+$- $e^-$ couples within $BiVO_4$.[37,38] Similarly, photogenerated holes from excited $WO_3$ are transferred into the valence band of $BiVO_4$, thus improving the charge separation properties within the $WO_3/BiVO_4$ coupled system.

Figure 4 shows the photoresponse of photoanodes measured in terms of IPCE (incident photon to current efficiency) spectra. The photocurrents obtained at different irradiation wavelengths were measured using a three electrodes cell and an applied potential of 1.23 V *vs*. RHE. Individual $WO_3$ and $BiVO_4$ electrodes exhibit a photocurrent onset at 470 nm and 520 nm, respectively, in line with their absorption spectra (Figure 1) and their band gap energy. Despite the higher absorption of the $BiVO_4$ film, the conversion efficiency was lower compared to that of $WO_3$, in agreement with the results of our linear sweep voltammetry experiments (Figure 3). The results of both types of measurement confirm that the low photoactivity of $BiVO_4$ is due to the poor charge carrier mobility of this material.[24,37,38] The combined $WO_3/BiVO_4$ electrode possesses the positive characteristics of both single semiconductors, *i.e.* the high conversion efficiency and charge carrier mobility typical of $WO_3$[39] and the good visible light harvesting properties of $BiVO_4$.

IPCE measurements were performed under low light intensity. In order to compare these values with the photocurrents recorded under AM 1.5G conditions in PEC experiments we integrated[40,41] the monochromatic quantum efficiency over the global sunlight spectral irradiance.[42] The integration gave values of 0.22, 0.33 and 0.89 mA $cm^{-2}$ for $WO_3$, $BiVO_4$ and $WO_3/BiVO_4$ photoanodes, respectively, that are little lower than photocurrents measured under simulated solar light irradiation (0.25, 0.35 and 1,0 mA $cm^{-2}$). The small difference in the corresponding values is ascribed to the photon flux dependent response of the photoelectrochemical cell.

**3.3. Transient absorption studies.** Transient absorption spectroscopy allowed us to probe the initial charge separation and charge transfer events from the changes in absorption following band gap excitation. This technique has been widely employed to investigate the dynamics of photogenerated charge carriers in photovoltaic,[43,44] photochemical[45] and photoelectrochemical materials. The samples were placed in an evacuated quartz cell and excited at 387 nm by a 130 fs FWHM laser pump pulse with 40 μJ $cm^{-2}$ energy density.

Previous studies revealed that electron trapping in $WO_3$ colloidal systems occurs rapidly,[46] when subjected to band gap excitation. In the present study no detectable signals were observed in transient absorption experiments with $WO_3$ films, thus confirming that the 387 nm excitation wavelength is not energetic enough to induce charge separation in $WO_3$ films.

Difference absorption spectra recorded following the excitation of the $BiVO_4$ film at different time delays after the pump pulse are presented in Figure 5A. These spectra exhibit a bleaching maximum at 450 nm corresponding to the depletion of ground state absorption. Two induced absorption bands are also observed in the 460-550 and 700-800 nm regions. The absorption-time profiles recorded at 420, 470 and 750 nm, corresponding to the three above-mentioned spectral regions, are shown in Figure 5B. All these three traces show initial fast recovery followed by a long-lived transient behavior.

The transient absorption features of $BiVO_4$ at 470 and 750 nm were also investigated to identify the charge carriers contributing to the absorption. An aqueous 0.5 M $Na_2SO_3$ solution was used as a hole scavenger. The film was immersed in the 0.5 M $Na_2SO_3$ solution for 24 h. The transient absorption measurements were then carried out with the semiconductor films in vacuum and in contact with the hole scavenger solution. The $\Delta A$ signals recorded at 470 nm and 750 nm with $BiVO_4$ films are presented in Figure 6A and 6B respectively. The decay signal recorded under vacuum at 750 nm was fitted by a biexponential decay model (Equation 1):

$$\Delta A_{\text{decay}} = A_1\, e^{(-t/\tau_1)} + A_2\, e^{(-t/\tau_2)} + \Delta A_0 \qquad (1)$$

where $\tau_1$ and $\tau_2$ are the time constants of the two decay components, $A_1$ and $A_2$ are their weights and $\Delta A_0$ is the offset (set as zero in the fitting).

The decay at 750 nm recorded in the presence of a $Na_2SO_3$ solution was fitted by a triexponential decay model (Equation 2).

$$\Delta A_{\text{decay}} = A_{\text{hs}}\, e^{(-t/\tau_{hs})} + A_1\, e^{(-t/\tau_1)} + A_2\, e^{(-t/\tau_2)} + \Delta A_0 \qquad (2)$$

In the presence of a hole scavenger a new decay pathway opens as $Na_2SO_3$ scavenges the holes, with a decay time $\tau_{\text{hs}}$ of 1.8 ± 0.1 ps and a $A_{\text{hs}}$ weight. The calculated fitting parameters are summarized in Table 1. Only the short components of the decay ($\tau_{\text{hs}}$ and $\tau_1$) are affected by the presence of $Na_2SO_3$, indicating that such signal decays can be ascribed to holes. Almost the same long time component $\tau_2$ was estimated both under vacuum and in the presence of the $Na_2SO_3$ solution. Therefore holes can be filled by the electron donor before being trapped, while trapped holes decay only by slow recombination with trapped electrons.

The faster decay in the presence of $Na_2SO_3$ solutions confirms the ability of $Na_2SO_3$ to scavenge photogenerated holes. Thus, we attribute the transient absorption with maxima at 470 and 750 nm to trapped holes in $BiVO_4$. This assignment is in agreement with earlier work

in which the induced absorbance in the transient spectrum was also attributed to trapped holes in $BiVO_4$.[31,47,48] The decrease in magnitude of $\Delta A$ with time in the present investigation offers insight into the loss of photogenerated holes in the $BiVO_4$ film. Kinetic analysis of these decay traces recorded at 470 nm allowed us to gain information on electron relaxation dynamics (Figure 7).

A model of carrier dynamics that includes recombination and trapping kinetics for electrons and holes in $BiVO_4$ was recently proposed by Ravensbergen *et al*.[48] Photogenerated holes, associated with the rise of a pronounced absorption at 475 nm and a broad absorption extending beyond 700 nm, were found to trap with a time constant of 5 ps. This event is followed by a biexponential decay with time constants of 40 ps and 2.5 ns arising from the recombination of electrons and holes.

Consistent with these results, we analyzed the transient $\Delta A$ signal (monitored at 470 nm) obtained after 387 nm excitation with a monoexponential growth and biexponential kinetic decay by fitting the transient absorption with Equation 3:

$$\Delta A = C\left[-e^{\left(-\frac{t}{\tau_{TR}}\right)} + A_1\, e^{\left(-\frac{t}{\tau_r}\right)} + A_2\, e^{\left(-\frac{t}{\tau_t}\right)}\right] \quad (3)$$

where $C$ is the magnitude of the transient absorption signal due to hole trapping and $\tau_{TR}$ is the hole trapping time constant, $\tau_r$ and $\tau_t$ are the shorter and longer decay components with weights $A_1$ and $A_2$, respectively. The growth of $\Delta A$ with a time constant $\tau_{TR}$ of 6.9 ± 0.6 ps and two decay components, of 24 ± 4 ps and 3.7 ± 0.2 ns were obtained (Table 2). The two decay lifetimes labeled $\tau_r$ and $\tau_t$ in Equation 3 are ascribed to the depletion of trapped holes due to electron-hole recombination competing with hot electron cooling and electron trapping, respectively.[48] As shown in Table 2, the initial decay process is responsible for *ca.* 50% of the decay. The relatively long-lived tail absorption corresponds to recombination between the trapped charge carriers.[48]

The 470 nm transient absorption decay of the $WO_3/BiVO_4$ composite system (Figure 7) was also fitted according to Equation 3 and the fitting parameters are also reported in Table 2. By comparing these parameters with those obtained with the $BiVO_4$ film, we notice that hole trapping occurs on a similar timescale ($\tau_{TR}$ = 6-7 ps). The shorter lifetime component $\tau_r$ exhibits a value of 18 ps for the $WO_3/BiVO_4$ system, which is shorter than that of pristine $BiVO_4$ ($\tau_r$ = 24 ps). Thus, as shown in Scheme 1, a new electron-hole recombination path is at work when $BiVO_4$ is in contact with $WO_3$, occurring on the same time scale and in competition with hot electrons cooling, *i.e.* their injection from $BiVO_4$ into $WO_3$, followed by back electron transfer from $WO_3$ to the $BiVO_4$ valence band. We are unable to determine which of these two steps is the rate limiting process dictating the disappearance of trapped holes in the $WO_3/BiVO_4$ coupled system. The longer hole decay component (with time constant $\tau_t \sim 3.8$ ns) does not appear to be markedly influenced by the presence of $WO_3$.

**3.4. Tracking electron injection with TH photocatalytic reduction as probe reaction.** Thionine (TH) has been widely used to probe the photocatalytic reduction properties of semiconductor particles and mesoscopic films.[49] By measuring the ratio of unreduced/reduced thionine it is also possible to determine the Fermi level of semiconductor materials.[46,50] The two-electron reduction of thionine to the colorless $TH^{2-}$ leuco form can be monitored following the bleaching of the TH absorption maximum at 606 nm (reactions 1 and 2).

$$MO_{(e^-)} + TH(blue) \rightarrow MO + TH^{-\bullet} \quad (1)$$

$$2\ TH^{-\bullet} \rightarrow TH^{2-}(colorless) + TH \quad (2)$$

with $MO_{(e^-)}$ representing an electron photopromoted in the conduction band of a metal oxide MO and $TH^{-\bullet}$ is the semireduced dye form. Metastable $TH^{-\bullet}$ undergoes quick disproportionation yielding the reduced colorless $TH^{2-}$ form.

The two electron-reduced form is stable under inert atmosphere, while it oxidizes reversibly to generate the parent dye when exposed to air. In the present study TH bleaching has been investigated in the presence of the $WO_3$, $BiVO_4$ and $WO_3/BiVO_4$ photoelectrodes under visible light irradiation ($\lambda > 400$ nm) without any applied bias. A blank experiment was also run using FTO in place of the semiconductor films.

With increased duration of visible light irradiation, a decrease in the absorption at 606 nm is observed (Figure 8A), as TH captures electrons from the semiconductor film and undergoes reduction. The reduction step was confirmed by exposure of the solution to air at the end of irradiation experiment. The color of the irradiated TH solution in the presence of semiconductor film completely recovered its original color after exposure to air (inset of Figure 8A), thus confirming the reversibility of dye reduction (Figure 8A). The extent of bleaching thus reflects the extent to which the dye can be reduced with different semiconductor films.

TH reduction in the presence of $WO_3$, $BiVO_4$ and of the combined $WO_3/BiVO_4$ films coated on FTO is shown in Figure 8B. Photoirradiated $BiVO_4$ film exhibits faster reduction ($k_{et}$ = 9. 2 $\times 10^{-3}$ $min^{-1}$) than the $WO_3$ film ($k_{et}$ = 2.7 $\times 10^{-3}$ $min^{-1}$). Interestingly with the coupled $WO_3/BiVO_4$ system the reduction rate ($k_{et}$ = 3.3 $\times$ $10^{-3}$ $min^{-1}$) is more similar to that obtained with $WO_3$ than to that obtained with $BiVO_4$. The variation in the electron transfer rate constant between $BiVO_4$ and $WO_3$ can be understood from the energy difference between the flat band potential of the semiconductor and the reduction potential of the dye.

The flat band potentials of the three materials were determined separately using photoelectrochemical measurements in the presence of $Na_2SO_3$ 0.5 M as hole scavenger (see Figure SI2 in the SI). The estimated onset potential at which we observe photocurrent is a good approximation of the flat band potential of the electrodes.[51] As expected, the flat band potentials of the single $WO_3$ and $BiVO_4$ films and of the coupled $WO_3/BiVO_4$ electrode were

found to be more negative in energy than the reduction potential of TH (0.064 V *vs.* NHE at pH 7).[52] Measurements on $BiVO_4$ and $WO_3/BiVO_4$ electrodes gave flat band values of 0.02 V and 0.19 V *vs.* RHE, respectively, indicating that the flat band potential (or apparent Fermi level[50]) in the coupled system is positively shifted by *ca.* 170 mV with respect to that of $BiVO_4$ and closer to that of $WO_3$ films (Scheme 2). Thus we can conclude that the driving force for the reduction step, as measured from the difference between the flat band potential of the semiconductor and the reduction potential of the electron acceptor, dictates the rate constant of electron reduction. While the decreased driving force for reduction of $WO_3/BiVO_4$ with respect to $BiVO_4$ results in the decreased electron transfer rate, similarity of the flat band potential of the $WO_3$ and $WO_3/BiVO_4$ system results in similar rate constants for electron transfer. By comparing the reduction rate constants and flat band potentials with $WO_3$ and $BiVO_4$ systems, we obtain further insights into the working principle of $WO_3/BiVO_4$ composite film.

## 4. CONCLUSIONS

$BiVO_4$, a photocatalyst with response in the visible can participate in reduction and oxidation process quite effectively. The charge separation in this system can be improved by coupling it with another oxide film (*e.g.* $WO_3$, $E_{CB}$ = +0.41 V *vs*. RHE) capable of accepting electrons from the conduction band of $BiVO_4$ ($E_{CB}$ = +0.02 V *vs*. RHE). While electrons lose their driving force for reduction, hole oxidation is significantly enhanced as evidenced by the enhanced photoconversion efficiency. The trapped holes, as characterized from transient absorption measurements, provide further insight into the excited state dynamics. A better understanding of the fast charge separation dynamics occurring in coupled oxides can further aid in designing tandem photocatalytic systems in which reduction and oxidation occur on the two different particles.

## ASSOCIATED CONTENT

### Supporting Information

XRPD of the electrodes, photoelectrochemical experiments in the presence of $Na_2SO_3$ as electron donor measured with the studied photoanodes and the diagram illustrating the band alignment between the two single oxides. This material is available free of charge via the Internet at http://pubs.acs.org.

## ACKNOWLEDGMENTS

We would like to thank Drs. Rabeka Alam and Jeff Christians for their assistance in recording FESEM images. IG and ES gratefully acknowledge financial support from Cariplo Foundation through the 2013-0615 grant to the project *Novel photocatalytic materials based on heterojunctions for solar energy conversion*. KGS and PVK acknowledge the support of the Division of Chemical Sciences, Geosciences, and Biosciences, Office of Basic Energy Sciences of the U.S. Department of Energy for their support through award DE- FC02-04ER15533. This is document no. NDRL 5081 from Notre Dame Radiation Laboratory.

## REFERENCES

(1) Kudo, A.; Miseki, Y. Heterogeneous Photocatalyst Materials for Water Splitting. *Chem. Soc. Rev.* **2009**, *38*, 253–278.

(2) Maeda, K.; Domen, K. Photocatalytic Water Splitting: Recent Progress and Future Challenges. *J. Phys. Chem. Lett.* **2010**, *1*, 2655–2661.

(3) Dozzi, M. V.; Selli, E. Doping $TiO_2$ with p-Block Elements: Effects on Photocatalytic Activity. *J. Photochem. Photobiol. C Photochem. Rev.* **2013**, *14*, 13–28.

(4) Zou, Z.; Ye, J.; Sayama, K.; Arakawa, H. Direct Splitting of Water under Visible Light Irradiation with an Oxide Semiconductor Photocatalyst. *Nature* **2001**, *414*, 625–627.

(5) Maeda, K.; Takata, T.; Hara, M.; Saito, N.; Inoue, Y.; Kobayashi, H.; Domen, K. GaN:ZnO Solid Solution as a Photocatalyst for Visible-Light-Driven Overall Water Splitting. *J. Am. Chem. Soc.* **2005**, *127*, 8286–8287.

(6) Park, Y.; McDonald, K. J.; Choi, K.-S. Progress in Bismuth Vanadate Photoanodes for Use in Solar Water Oxidation. *Chem. Soc. Rev.* **2013**, *42*, 2321–2337.

(7) Bignozzi, C. A.; Caramori, S.; Cristino, V.; Argazzi, R.; Meda, L.; Tacca, A. Nanostructured Photoelectrodes Based on $WO_3$: Applications to Photooxidation of Aqueous Electrolytes. *Chem. Soc. Rev.* **2013**, *42*, 2228–2246.

(8) Grätzel, M. Photoelectrochemical Cells. *Nature* **2001**, *414*, 338–344.

(9) Santato, C.; Odziemkowski, M.; Ulmann, M.; Augustynski, J. Crystallographically Oriented Mesoporous $WO_3$ Films: Synthesis, Characterization, and Applications. *J. Am. Chem. Soc.* **2001**, *123*, 10639–10649.

(10) Kudo, A.; Omori, K.; Kato, H. A Novel Aqueous Process for Preparation of Crystal Form-Controlled and Highly Crystalline $BiVO_4$ Powder from Layered Vanadates at Room Temperature and Its Photocatalytic and Photophysical Properties. *J. Am. Chem. Soc.* **1999**, *121*, 11459–11467.

(11) Walsh, A.; Yan, Y.; Huda, M. N.; Al-Jassim, M. M.; Wei, S. Band Edge Electronic Structure of $BiVO_4$: Elucidating the Role of the Bi s and V d Orbitals. *Chem. Mater.* **2009**, *21*, 547–551.

(12) Eisenberg, D.; Ahn, H. S.; Bard, A. J. Enhanced Photoelectrochemical Water Oxidation on Bismuth Vanadate by Electrodeposition of Amorphous Titanium Dioxide. *J. Am. Chem. Soc.* **2014**, *136*, 14011–14014.

(13) Mcdowell, M. T.; Lichterman, M. F.; Spurgeon, J. M.; Hu, S.; Sharp, I. D.; Brunschwig, B. S.; Lewis, N. S. Improved Stability of Polycrystalline Bismuth Vanadate Photoanodes by Use of Dual-Layer Thin $TiO_2$/Ni Coatings. *J. Phys. Chem. C* **2014**, *118*, 19618–19624.

(14) Park, H. S.; Kweon, K. E.; Ye, H.; Paek, E.; Hwang, G. S.; Bard, A. J. Factors in the Metal Doping of $BiVO_4$ for Improved Photoelectrocatalytic Activity as Studied by Scanning Electrochemical Microscopy and First-Principles Density-Functional Calculation. *J. Phys. Chem. C* **2011**, *115*, 17870–17879.

(15) Abdi, F. F.; Han, L.; Smets, A. H. M.; Zeman, M.; Dam, B.; van de Krol, R. Efficient Solar Water Splitting by Enhanced Charge Separation in a Bismuth Vanadate-Silicon Tandem Photoelectrode. *Nat. Commun.* **2013**, *4*, 2195.

(16) Huang, Z.-F.; Pan, L.; Zou, J.-J.; Zhang, X.; Wang, L. Nanostructured Bismuth Vanadate-Based Materials for Solar-Energy-Driven Water Oxidation: A Review on Recent Progress. *Nanoscale* **2014**, *6*, 14044–14063.

(17) Zhang, L.; Reisner, E.; Baumberg, J. J. Al-Doped ZnO Inverse Opal Networks as Efficient Electron Collectors in $BiVO_4$ Photoanodes for Solar Water Oxidation. *Energy Environ. Sci.* **2014**, *7*, 1402–1408.

(18) Zhou, M.; Bao, J.; Xu, Y.; Zhang, J.; Xie, J.; Guan, M.; Wang, C.; Wen, L.; Lei, Y.; Xie, Y. Photoelectrodes Based upon Mo:$BiVO_4$ Inverse Opals for Photoelectrochemical Water Splitting. *ACS Nano* **2014**, *8*, 7088–7098.

(19) Kim, T. W.; Choi, K.-S. Nanoporous $BiVO_4$ Photoanodes with Dual-Layer Oxygen Evolution Catalysts for Solar Water Splitting. *Science* **2014**, *343*, 990–994.

(20) Pilli, S. K.; Furtak, T. E.; Brown, L. D.; Deutsch, T. G.; Turner, J. A.; Herring, A. M. Cobalt-Phosphate (Co-Pi) Catalyst Modified Mo-Doped $BiVO_4$ Photoelectrodes for Solar Water Oxidation. *Energy Environ. Sci.* **2011**, *4*, 5028–5034.

(21) Zhong, D. K.; Choi, S.; Gamelin, D. R. Near-Complete Suppression of Surface Recombination in Solar Photoelectrolysis by " Co-Pi " Catalyst-Modified W:$BiVO_4$. *J. Am. Chem. Soc.* **2011**, *133*, 18370–18377.

(22) Chatchai, P.; Murakami, Y.; Kishioka, S.; Nosaka, A. Y.; Nosaka, Y. Efficient Photocatalytic Activity of Water Oxidation over $WO_3$/$BiVO_4$ Composite under Visible Light Irradiation. *Electrochim. Acta* **2009**, *54*, 1147–1152.

(23) Su, J.; Guo, L.; Bao, N.; Grimes, C. A. Nanostructured WO/$BiVO_4$ Heterojunction Films for Efficient Photoelectrochemical Water Splitting. *Nano Lett.* **2011**, *11*, 1928–1933.

(24) Hong, S. J.; Lee, S.; Jang, J. S.; Lee, J. S. Heterojunction $BiVO_4/WO_3$ Electrodes for Enhanced Photoactivity of Water Oxidation. *Energy Environ. Sci.* **2011**, *4*, 1781–1787.

(25) Fujimoto, I.; Wang, N.; Saito, R.; Miseki, Y.; Gunji, T.; Sayama, K. $WO_3/BiVO_4$ Composite Photoelectrode Prepared by Improved Auto-Combustion Method for Highly Efficient Water Splitting. *Int. J. Hydrogen Energy* **2014**, *39*, 2454–2461.

(26) Durrant, J. R. Molecular Approaches to Solar Energy Conversion: The Energetic Cost of Charge Separation from Molecular-Excited States. *Philos. Trans. R. Soc. A* **2013**, *371*, 20120195.

(27) Pihosh, Y.; Turkevych, I.; Mawatari, K.; Asai, T.; Hisatomi, T.; Uemura, J.; Tosa, M.; Shimamura, K.; Kubota, J.; Domen, K.; Kitamori, T. Nanostructured $WO_3/BiVO_4$ Photoanodes for Efficient Photoelectrochemical Water Splitting. *Small* **2014**, *10*, 3692–3699.

(28) Tang, J.; Durrant, J. R.; Klug, D. R. Mechanism of Photocatalytic Water Splitting in $TiO_2$. Reaction of Water with Photoholes, Importance of Charge Carrier Dynamics, and Evidence for Four-Hole Chemistry. *J. Am. Chem. Soc.* **2008**, *130*, 13885–13891.

(29) Pendlebury, S. R.; Barroso, M.; Cowan, A. J.; Sivula, K.; Durrant, J. R.; Tang, J.; Grätzel, M. Dynamics of Photogenerated Holes in Nanocrystalline $\alpha$-$Fe_2O_3$ Electrodes for Water Oxidation Probed by Transient Absorption Spectroscopy. *Chem. Commun.* **2011**, *47*, 716–718.

(30) Pesci, F. M.; Cowan, A. J.; Alexander, B. D.; Durrant, J. R.; Klug, D. R. Charge Carrier Dynamics on Mesoporous $WO_3$ during Water Splitting. *J. Phys. Chem. Lett.* **2011**, *2*, 1900–1903.

(31) Ma, Y.; Pendlebury, S. R.; Reynal, A.; Le Formal, F.; Durrant, J. R. Dynamics of Photogenerated Holes in Undoped $BiVO_4$ Photoanodes for Solar Water Oxidation. *Chem. Sci.* **2014**, *5*, 2964–2973.

(32) Cherepy, N. J.; Liston, D. B.; Lovejoy, J. A.; Deng, H.; Zhang, J. Z. Ultrafast Studies of Photoexcited Electron Dynamics in γ- and α-$Fe_2O_3$ Semiconductor Nanoparticles. *J. Phys. B* **1998**, *102*, 770–776.

(33) Pendlebury, S. R.; Wang, X.; Le Formal, F.; Cornuz, M.; Kafizas, A.; Tilley, S. D.; Grätzel, M.; Durrant, J. R. Ultrafast Charge Carrier Recombination and Trapping in Hematite Photoanodes under Applied Bias. *J. Am. Chem. Soc.* **2014**, *136*, 9854–9857.

(34) Kronawitter, C. X.; Vayssieres, L.; Shen, S.; Guo, L.; Wheeler, D. A.; Zhang, J. Z.; Antoun, B. R.; Mao, S. S. A Perspective on Solar-Driven Water Splitting with All-Oxide Hetero-Nanostructures. *Energy Environ. Sci.* **2011**, *4*, 3889–3899.

(35) Su, J.; Guo, L.; Yoriya, S.; Grimes, C. A. Aqueous Growth of Pyramidal-Shaped $BiVO_4$ Nanowire Arrays and Structural Characterization : Application to Photoelectrochemical Water Splitting. *Cryst. Growth Des.* **2010**, *10*, 856–861.

(36) Luo, W.; Yang, Z.; Li, Z.; Zhang, J.; Liu, J.; Zhao, Z.; Wang, Z.; Yan, S.; Yu, T.; Zou, Z. Solar Hydrogen Generation from Seawater with a Modified $BiVO_4$ Photoanode. *Energy Environ. Sci.* **2011**, *4*, 4046–4051.

(37) Kay, A.; Cesar, I.; Grätzel, M. New Benchmark for water photoxidation by nanostructured α-$Fe_2O_3$ films. *J. Am. Chem. Soc.* **2006**, 128, 15714-15721

(38) Christians J. A.; Manser J. S.; Kamat P. V. Best Practices in Perovskite Solar Cell Efficiency Measurements. Avoiding the Error of Making Bad Cells Look Good. *J. Phys. Chem. Lett.* **2015**, *6*, 852-857

(39) http://rredc.nrel.gov/solar/spectra/am1.5/

(40) Abdi, F. F.; Savenije, T. J.; May, M. M.; Dam, B.; van de Krol, R. The Origin of Slow Carrier Transport in $BiVO_4$ Thin Film Photoanodes. *J. Phys. Chem. Lett.* **2013**, *4*, 2752–2757.

(41) Abdi, F. F.; van de Krol, R. Nature and Light Dependence of Bulk Recombination in Co-Pi- Catalyzed $BiVO_4$ Photoanodes. *J. Phys. Chem. C* **2012**, *116*, 9398–9404.

(42) Butler, M. A. Photoelectrolysis and Physical Properties of the Semiconducting Electrode $WO_3$. *J. Appl. Phys.* **1977**, *48*, 1914–1920.

(43) Christians, J. A.; Leighton, D. T.; Kamat, P. V. Rate Limiting Interfacial Hole Transfer in $Sb_2S_3$ Solid-State Solar Cells. *Energy Environ. Sci.* **2014**, *7*, 1148–1158.

(44) Jara, D. H.; Yoon, S. J.; Stamplecoskie, K. G.; Kamat, P. V. Size-Dependent Photovoltaic Performance of $CuInS_2$ Quantum Dot-Sensitized Solar Cells. *Chem. Mater.* **2014**, *26*, 7221–7228.

(45) Stamplecoskie, K. G.; Chen, Y.-S.; Kamat, P. V. Excited-State Behavior of Luminescent Glutathione-Protected Gold Clusters. *J. Phys. Chem. C* **2014**, *118*, 1370–1376.

(46) Bedja, I.; Hotchandani, S.; Kamat, P. V. Photoelectrochemistry of Quantized $WO_3$ Colloids. Electron Storage, Electrocbromic, and Photoelectrochromic Effects. *J. Phys. Chem.* **1993**, *97*, 11064–11070.

(47) Aiga, N.; Jia, Q.; Watanabe, K.; Kudo, A.; Sugimoto, T.; Matsumoto, Y. Electron–Phonon Coupling Dynamics at Oxygen Evolution Sites of Visible-Light-Driven Photocatalyst: Bismuth Vanadate. *J. Phys. Chem. C* **2013**, *117*, 9881–9886.

(48) Ravensbergen, J.; Abdi, F. F.; van Santen, J. H.; Frese, R. N.; Dam, B.; van de Krol, R.; Kennis, J. T. M. Unraveling the Carrier Dynamics of $BiVO_4$: A Femtosecond to Microsecond Transient Absorption Study. *J. Phys. Chem. C* **2014,** *118*, 27793-27800.

(49) Kamat, P. V., Photoelectrochemistry in Colloidal Systems: Interfacial Electron Transfer Between Colloidal $TiO_2$ and Thionine in Acetonitrile. *J. Photochem.* **1985,** *28*, 513-524.

(50) Subramanian, V.; Wolf, E. E.; Kamat, P. V. Catalysis with $TiO_2$/gold Nanocomposites. Effect of Metal Particle Size on the Fermi Level Equilibration. *J. Am. Chem. Soc.* **2004**, *126*, 4943–4950.

(51) Chen, Z.; Jaramillo, T. F.; Deutsch, T. G.; Kleiman-Shwarsctein, A.; Forman, A. J.; Gaillard, N.; Garland, R.; Takanabe, K.; Heske, C.; Sunkara, M.; et al. Accelerating Materials Development for Photoelectrochemical Hydrogen Production: Standards for Methods, Definitions, and Reporting Protocols. *J. Mater. Res.* **2011**, *25*, 3–16.

(52) Kamat, P. V. Photoelectrochemistry in Colloidal Systems. *J. Chem. Soc. Faraday Trans. 1* **1985**, *81*, 509–518.

**Table 1. Fitting parameters of the $\Delta A$ signals recorded at 750 nm with the $BiVO_4$ film under vacuum and in the presence of $Na_2SO_3$ as hole scavenger.**

| | $BiVO_4$ | $BiVO_4$ in $Na_2SO_3$ |
|---|---|---|
| $A_{hs}$ | | 0.51 ± 0.02 |
| $\tau_{hs}$ (ps) | | 1.85 ± 0.15 |
| $A_1$ | 0.38 ± 0.02 | 0.201 ± 0.013 |
| $\tau_1$ (ps) | 38 ± 2 | 54 ± 9 |
| $A_2$ | 0.620 ± 0.006 | 0.288 ± 0.008 |
| $\tau_2$ (ps) | 3373 ± 128 | 3377 ± 433 |
| $\chi^{2a}$ | $4.8\ 10^{-4}$ | $8.3\ 10^{-4}$ |

[a] The $\chi^2$ (chi square) term is used to estimate the reliability of the fitting model and the experimental data; the fit is good if $\chi^2$ is minimized.

**Table 2. Fitting parameters (Equation 1) for the $\Delta A$ signals at 470 nm recorded with the $BiVO_4$ and $WO_3/BiVO_4$ films**

| | $BiVO_4$ | $WO_3/BiVO_4$ |
|---|---|---|
| $\tau_{TR}$ (ps) | 6.9 ± 0.6 | 6.2 ± 1.3 |
| $A_1$ | 0.51 ± 0.04 | 0.63 ± 0.07 |
| $\tau_r$ (ps) | 24 ± 4 | 18 ± 5 |
| $A_2$ | 0.49 ± 0.06 | 0.37 ± 0.13 |
| $\tau_t$ (ps) | 3708 ± 163 | 3907 ± 379 |
| $\chi^{2a}$ | $7.0\ 10^{-4}$ | $2.2\ 10^{-3}$ |

[a] The $\chi^2$ (chi square) term is used to estimate the reliability of the fitting model and the experimental data; the fit is good if $\chi^2$ is minimized.

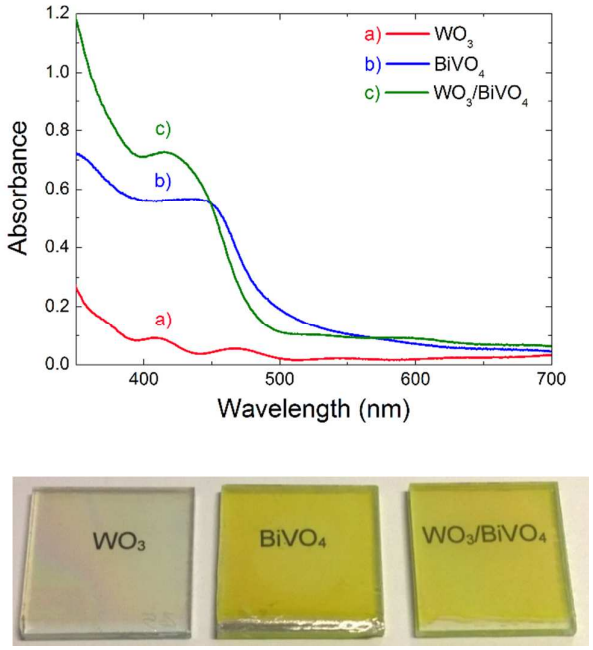


**Figure 1.** Absorption spectra (top) and photographs (bottom) of the oxide films deposited on conducting glass (FTO) electrodes: a) $WO_3$, b) $BiVO_4$ and c) $WO_3/BiVO_4$ films.

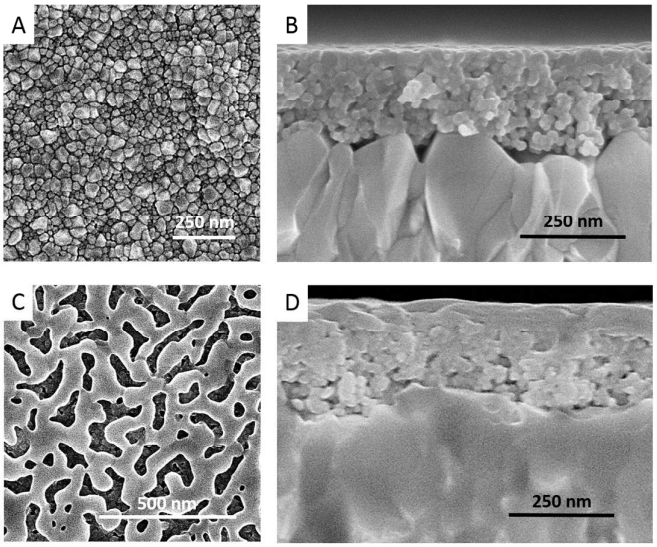


**Figure 2.** FESEM images of (A,C) $WO_3$ and (B,D) $WO_3/BiVO_4$ films deposited on conducting glass electrodes The images are presented as top view (A,B) and cross sectional view (C,D).

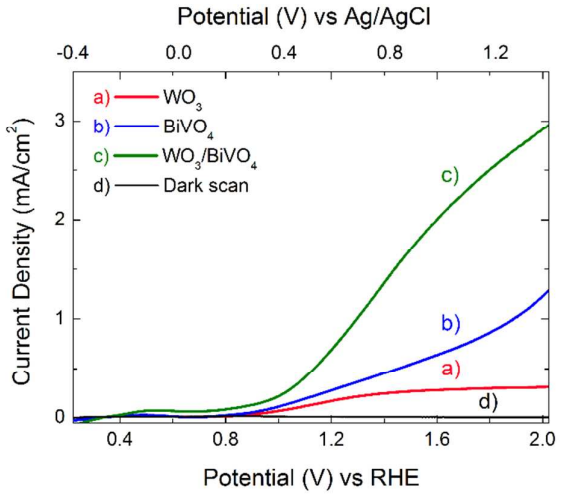


**Figure 3.** Linear sweep voltammetry under AM 1.5G irradiation of the a) $WO_3$, b) $BiVO_4$ and c) $WO_3/BiVO_4$ photoanodes, recorded in $Na_2SO_4$ 0.5 M aqueous solution, with a scan rate of 10 mV $s^{-1}$; d) dark current (black line) measured with the $WO_3/BiVO_4$ film.

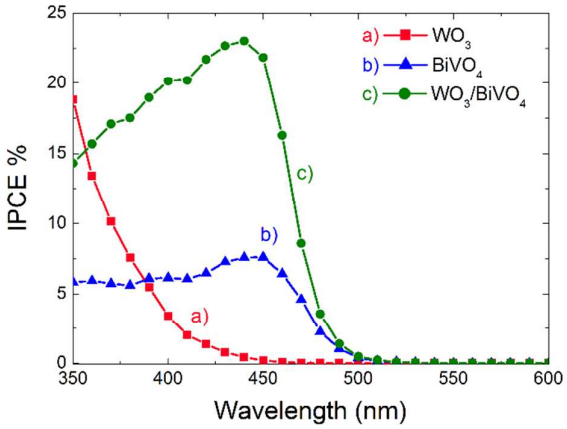


**Figure 4.** Incident photon to current efficiency (IPCE) measured with the a) $WO_3$, b) $BiVO_4$ and c) $WO_3$-$BiVO_4$ electrodes, in 0.5 M $Na_2SO_4$ aqueous solution, at 1.23 V *vs.* RHE.

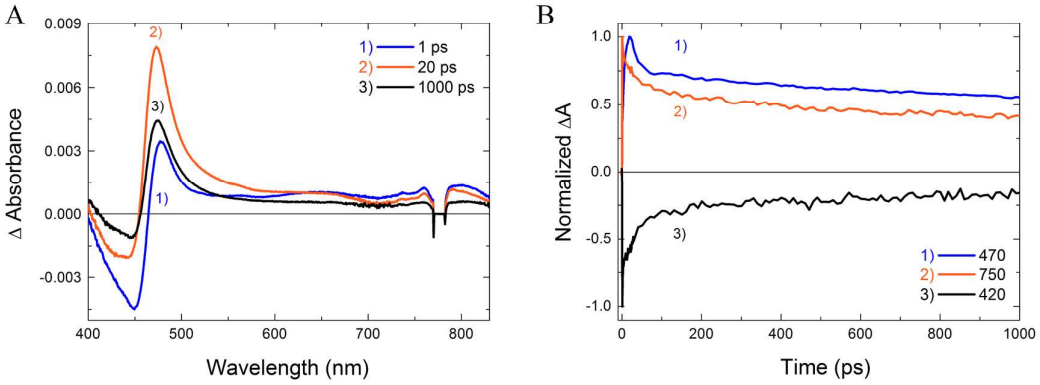


**Figure 5.** (A) Transient absorption spectra of the $BiVO_4$ film recorded 1) 1 ps, 2) 20 ps and 3) 1000 ps after the pump pulse. The spectra could be divided into two regions: 400-460 nm (bleaching due to ground state depopulation); 460-850 nm (absorption assigned to holes). (B) Transient absorption decay of the $BiVO_4$ film. Traces 1) and 2) correspond to the decay of trapped holes, monitored at 470 and 750 nm, respectively, line 3) corresponds to the bleaching recovery recorded at 420 nm.

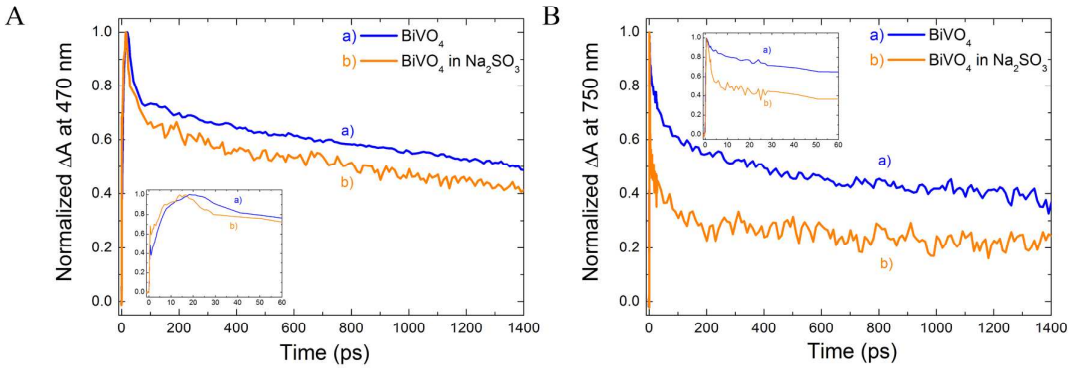


**Figure 6.** Absorption decay profiles recorded at (A) 470 nm and (B) 750 nm for the $BiVO_4$ film, a) under vacuum and b) in the presence of 0.5 M $Na_2SO_3$ aqueous solution, as electron donor. The insets show the magnification of the signals in the first 60 ps after excitation.

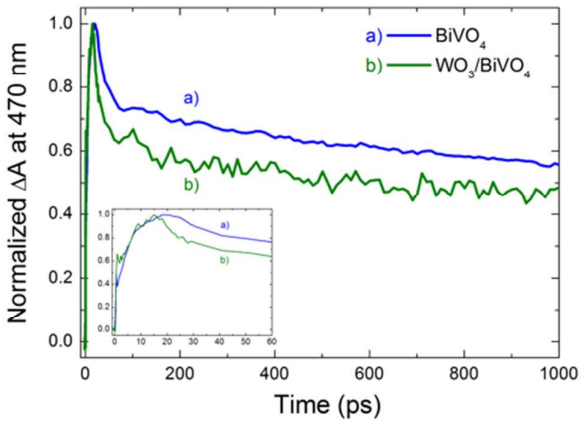


**Figure 7.** Transient absorption decay at 470 nm monitored for a) the $BiVO_4$ and b) the $WO_3/BiVO_4$ heterojunction electrodes. In the case of the coupled system the faster decay is due to holes filling by back transferred electrons from the conduction band of $WO_3$ to the valence band of $BiVO_4$. Inset: magnification of the ~~Δ~~*A* signal at short time after the laser pulse.

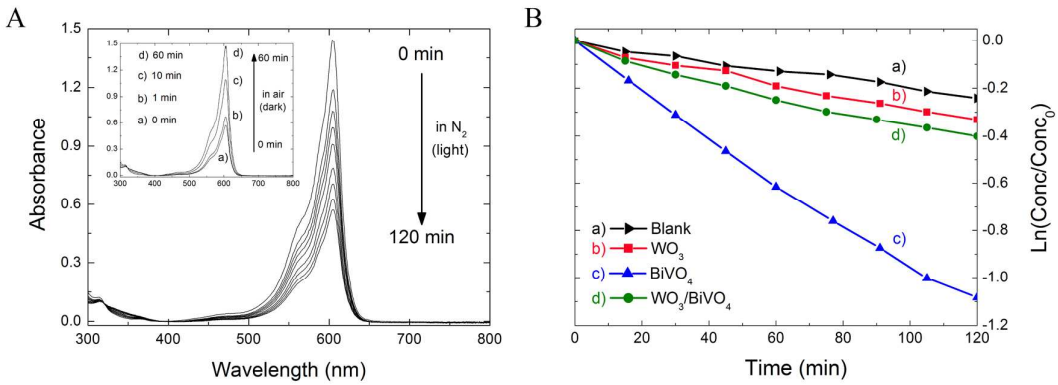


**Figure 8.** (A) Absorption spectra recorded during a TH photoreduction experiment in the presence of $BiVO_4$. Inset: absorption spectra recorded at different time after opening the cuvette to air after the end of irradiation: the solution recovered the blue coloration of oxidized TH. (B) Logarithmic plot of the concentration decay of TH in contact with $WO_3$, $BiVO_4$ and $WO_3/BiVO_4$ films irradiated at 400 nm. The blank experiment a) was run with FTO placed in the cuvette, in contact with the TH solution.

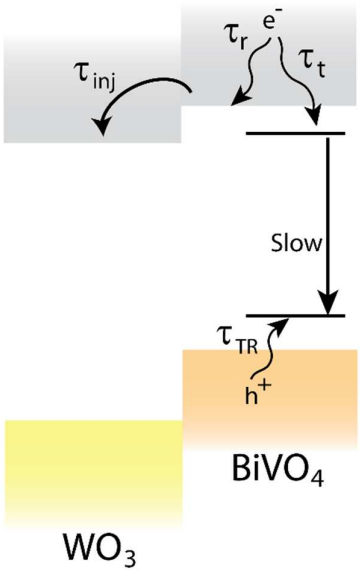


**Scheme 1.** Proposed charge carrier transitions involving $BiVO_4$ and $WO_3$. For the different time constants labelling, please refer to the text.

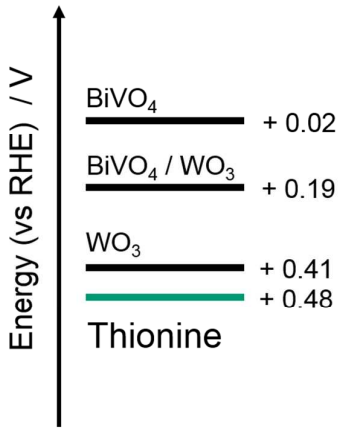


**Scheme 2.** Apparent energy of semiconductors Fermi levels (see SI for details)

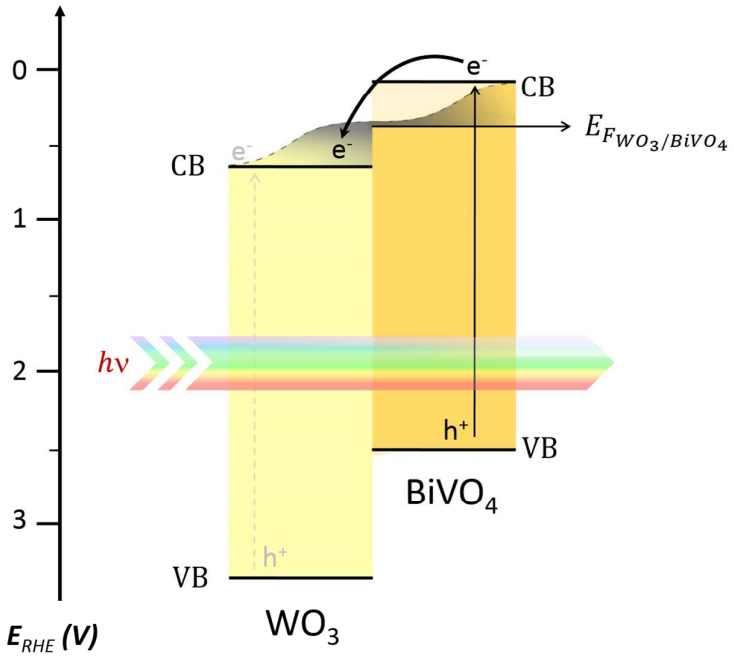


Table of Contents (TOC) Graphic